

# Comparison of high-mode predictive simulations using Mixed Bohm/gyro-Bohm and Multi-Mode (MMM95) transport models

David Hannum, Glenn Bateman, Jon Kinsey, Arnold H. Kritz, Thawatchai Onjun, and Alexei Pankin

*Lehigh University Physics Department, 16 Memorial Drive East, Bethlehem, Pennsylvania 18015*

(Received 18 May 2000; accepted 15 September 2000)

Two different transport models—the Mixed Bohm/gyro-Bohm [Joint European Torus (JET)] model [Erba *et al.*, *Plasma Phys. Controlled Fusion* **39**, 261 (1997)] and the Multi-Mode model (MMM95) [Bateman *et al.*, *Phys. Plasmas* **5**, 1793 (1998)]—are used in predictive transport simulations of 22 high-mode discharges. Fourteen discharges that include systematic scans in normalized gyroradius ( $\rho_*$ ), plasma pressure ( $\beta$ ), collisionality, and isotope mass in the JET tokamak [Rebut *et al.*, *Nucl. Fusion* **25**, 1011 (1985)] and eight discharges that include scans in  $\rho_*$ , elongation ( $\kappa$ ), power, and density in the DIII-D tokamak [J. L. Luxon and L. G. Davis, *Fusion Technol.* **8**, 441 (1985)] are considered. When simulation temperature and density profiles are compared with processed experimental data from the International Profile Database, it is found that the results with either the JET or MMM95 transport model match experimental data about equally well. With either model, the average normalized rms deviation is approximately 10%. In the simulations carried out using the JET model, the component of the model with Bohm scaling (which is proportional to gyroradius) dominates over much of the plasma. In contrast, the MMM95 model has purely gyro-Bohm scaling (proportional to gyroradius squared). In spite of the differences in the underlying scaling of these transport models, both models reproduce the global confinement scalings observed in the scans equally well. These results are explained by changes in profile shapes from one end of each scan to the other. These changes in the profile shapes are caused by changes in boundary conditions, heating and particle source profiles, large scale instabilities, and transport. © 2001 American Institute of Physics. [DOI: 10.1063/1.1338534]

## I. INTRODUCTION

Predictive transport simulations using two different transport models are compared with each other and with experimental data in this paper. One of the models used in this paper is the Multi-Mode transport model (MMM95), which consists of a combination of theory-based models.<sup>1</sup> The other model is the empirical Mixed Bohm/gyro-Bohm (Joint European Torus, JET) transport model.<sup>2</sup> The temperature and density profiles predicted by simulations using each of these models have been shown to match experimental data from tokamaks.<sup>3–7</sup> However, the two models have very different scalings with respect to plasma parameters and different dependencies on the shapes of the plasma profiles. The models are compared in this paper by using them in pairs of predictive simulations that are set up to be identical in every respect other than the choice of the transport model.

One of the key differences between the MMM95 and JET models is the gyroradius scaling of their diffusivities ( $\chi$ ). While the MMM95 model has a purely gyro-Bohm scaling ( $\chi \propto \rho_s^2 c_s / R$ ), the JET has a Bohm-dominant scaling ( $\chi \propto \rho_s c_s$ ) in simulations of large tokamak plasmas (see Table I for notation and definitions). In systematic gyroradius scans, the magnetic field strength is varied from discharge to discharge to vary  $\rho_s / a$ , while the density, temperature, and current are varied to hold  $\beta$ , dimensionless collisionality, and magnetic  $q$  fixed. If the shapes of the profiles were held completely fixed in gyroradius scans, the

magnetic field scaling of gyro-Bohm models would be  $\chi \propto B_T^{-1}$  while the scaling of Bohm dominated models would be  $\chi \propto B_T^{-1/3}$ .<sup>6</sup> However, the shapes of the plasma profiles do change from one end of each scan to the other, and these changes in profile shape have a significant effect on the relation between the scaling of global confinement and the underlying scaling of the particular transport model.

Previous work<sup>6,4</sup> has shown that changes in the shapes of the temperature and density profiles ( $T_i, T_e, n_e$ ) caused by changes in boundary conditions or by changes in sources or sinks, from one end of each scan to the other, can have an effect on the global confinement scaling in simulations of *L*-mode (low mode) and *H*-mode (high mode) plasmas. For example, in *L*-mode plasmas, variation in edge neutral penetration depth causes the  $n_e$  profiles to change near the edge of the plasma, which changes the scaling of  $\chi$ .<sup>6</sup> As a result of these changes in plasma profile, the Multi-Mode model, with its pure gyro-Bohm scaling, can produce a global energy confinement scaling that is only weakly dependent of magnetic field (i.e., less dependent than Bohm scaling on magnetic field). In simulations of *H*-mode plasmas,<sup>4</sup> it is found that the height of the pedestal at the edge of each *H*-mode plasma has a large effect on the shape of the temperature and density profiles and, consequently, the height of the pedestal has a large effect on global confinement scaling. Simulations of isotope scans in ELMy JET *H*-mode plasmas (high mode plasmas with edge localized modes) show how

TABLE I. Notation.

Variable	Units	Meaning
$a$	m	Minor radius (half-width) of plasma
$B_T$	T	Vacuum toroidal magnetic field at major radius $R$ along flux surface
$c_s$	m/s	$[k_b T_e / m_i]^{1/2}$ speed of sound
$D$	m <sup>2</sup> /s	Effective charged particle diffusivity
		Charged particle flux divided by density gradient
$e$	C	Electron charge
$I_p$	MA	Toroidal plasma current
$k_b$		Conversion from keV to joules
$m_i$	kg	Average ion mass
$n_e$	m <sup>-3</sup>	Electron density
$P_{NB}$	MW	Neutral beam injection power
$q$		Magnetic $q$ value
$r$	m	Minor radius (half-width) of each flux surface
$R$	m	Major radius to geometric center of flux surface
$t_{saw}$	s	Time of last sawtooth crash
$T_e$	keV	Electron temperature
$T_i$	keV	Ion temperature
$W_{th}$	MJ	Thermal plasma energy
$W_{tot}$	MJ	Total plasma energy (including fast ions)
$Z_{eff}$		$\sum_s n_s Z_s^2 / n_e$ summed over each species
$\beta$		Beta [ $W_{th} / (B_T^2 / 2\mu_0)$ ]
$\chi$	m <sup>2</sup> /s	Effective thermal diffusivity
		Heat flux divided by density time temperature gradient
$\delta$		Plasma triangularity
$\kappa$		Plasma elongation
$\nu_*$		Collision frequency divided by bounce frequency
$\rho_s$	m	Gyroradius [ $c_s m_i / (e B_T)$ ]
$\rho_*$		Normalized gyroradius ( $\rho_s / a$ )
$\tau_E$	s	Total energy confinement time ( $W_{tot} / P_{NB}$ )
$\tau_{th}$	s	Thermal energy confinement time ( $W_{th} / P_{loss}$ )
		where $P_{loss}$ is power lost through edge of plasma

this effect can influence the confinement of discharges in a systematic way.<sup>3</sup>

Motivated by these studies, 22  $H$ -mode discharges taken from the International Profile Database<sup>8</sup> were simulated using both the MMM95 and the JET transport modules in the BALDUR code.<sup>9</sup> Of the 22  $H$ -mode plasmas, 14 are taken from JET<sup>2</sup> experiments and 8 are taken from DIII-D<sup>10</sup> experiments. The JET series includes systematic scans of the normalized gyroradius ( $\rho_*$ ), normalized plasma pressure ( $\beta$ ), collisionality ( $\nu_*$ ), and isotope mass. In addition, one of the JET discharges is referred to as an ‘‘identity shot,’’ JET 33465, which is part of a series of experiments designed to test  $\rho_*$  scaling across various tokamaks. The DIII-D series includes systematic scans of  $\rho_*$ , elongation ( $\kappa$ ), and plasma density and power.

The transport models are described in Sec. II. Details of the experimental JET and DIII-D discharges are given in Sec. III. Section IV presents a statistical analysis of the temperature and density profiles produced by simulations using the JET and MMM95 transport models compared with experimental data. In addition, an analysis of the physical processes in the simulations that produce the observed scaling in each scan is also presented in Sec. IV. Simulations of the International Thermonuclear Experimental Reactor (ITER) tokamak reactor design are presented in Sec. V. Conclusion are given in Sec. VI.

## II. TRANSPORT MODELS

The MMM95 version of the multimode model is described in detail in Ref. 1 and is available as a National Transport Code Collaboration (NTCC) computer code module at the website <http://w3.pppl.gov/NTCC>. The MMM95 model has been used extensively to simulate  $H$ -mode plasmas<sup>3,4,11</sup> as well as  $L$ -mode and other plasmas such as hot ion modes.<sup>1,5,6,12,13</sup> The MMM95 transport model is a pure gyro-Bohm model.

The version of the JET model that is used in this paper is described in Ref. 2. Both the electron and ion thermal diffusivities consist of two terms. One term has Bohm scaling

$$\chi^{\text{Bohm}} \equiv \rho_s c_s q^2 \frac{a(dp_e/dr)}{p_e} \Delta T_e, \quad (1)$$

while the other term has gyro-Bohm scaling

$$\chi^{\text{gyro-Bohm}} \equiv \frac{\rho_s^2 c_s a(dT_e/dr)}{a T_e}. \quad (2)$$

The notation is described in Table I. In the Bohm diffusivity expression,  $\Delta T_e$  is a finite difference approximation to the normalized temperature electron temperature difference at the plasma edge

$$\Delta T_e \equiv \frac{T_e(r/a=0.8) - T_e(r/a=1)}{T_e(r/a=1)}. \quad (3)$$

The resulting anomalous ion and electron thermal diffusivities are constructed from the sum of these Bohm and gyro-Bohm terms, with empirically determined coefficients<sup>2</sup>

$$\chi_i^{\text{JET}} = 1.6 \times 10^{-4} \chi^{\text{Bohm}} + 1.75 \times 10^{-2} \chi^{\text{gyro-Bohm}}, \quad (4)$$

$$\chi_e^{\text{JET}} = 8 \times 10^{-5} \chi^{\text{Bohm}} + 3.5 \times 10^{-2} \chi^{\text{gyro-Bohm}}, \quad (5)$$

and the hydrogenic and impurity charged particle diffusivity is given by

$$D^{\text{JET}} \propto \frac{\chi_i \chi_e}{\chi_i + \chi_e}. \quad (6)$$

All the simulations are carried out using the time-dependent BALDUR integrated predictive transport code <http://www.physics.lehigh.edu/baldur/index.htm>.<sup>9</sup> In each simulation, either the JET or the MMM95 transport model is used together with neoclassical transport. Each simulation follows the time evolution of the ion temperature, electron temperature, hydrogenic density, impurity density and  $q$  profile, given boundary conditions from experimental data.

## III. $H$ -MODE EXPERIMENTAL DATA

All the experimental data from the 22  $H$ -mode discharges considered in this paper are taken from the International Profile Database.<sup>8</sup> All of this data was processed by the TRANSP code, a time-dependent transport analysis code <http://w3.pppl.gov/transp/>.<sup>14</sup>

### A. JET discharges

The 14 JET  $H$ -mode discharges consist of 2 pairs of normalized gyroradius ( $\rho_*$ ) scans, a  $\beta$  scan, a collisionality

TABLE II. Major plasma parameters for the JET discharges.

Tokamak discharge: Type	JET 33131 Low $\rho_*$	JET 33140 High $\rho_*$	JET 33465 Identity	JET 35156 Low $\rho_*$	JET 35171 High $\rho_*$	JET 37718 High $\nu_*$	JET 37728 Low $\nu_*$	JET 38407 Low $\beta$	JET 38415 High $\beta$
$R$ (m)	2.94	2.93	2.87	2.87	2.88	2.94	2.92	2.91	2.88
$a$ (m)	0.94	0.92	0.95	0.93	0.94	0.93	0.96	0.94	0.97
$\kappa$	1.70	1.56	1.55	1.56	1.58	1.58	1.64	1.60	1.55
$\delta$	0.28	0.26	0.19	0.11	0.24	0.13	0.20	0.16	0.11
$B_T$ (T)	3.13	1.77	1.10	2.17	1.09	2.11	2.71	1.59	1.84
$I_p$ (MA)	2.83	1.61	1.04	2.05	1.01	1.97	2.57	1.47	1.67
$\bar{n}_e$ ( $10^{19} \text{ m}^{-3}$ )	7.10	3.65	3.26	5.44	2.44	4.54	4.90	3.05	4.02
$Z_{\text{eff}}$	1.92	1.66	1.52	1.25	1.10	1.93	1.76	2.09	2.06
$P_{\text{NB}}$ (MW)	18.0	5.80	2.77	8.60	2.91	9.70	13.3	5.60	15.7
$\rho_*(0)$ ( $10^{-3} \text{ m}$ )	5.11	7.59	7.77	4.96	9.66	6.02	6.07	8.34	7.42
$\tau_{\text{th}}$ (s)	0.26	0.37	0.37	0.40	0.24	0.29	0.24	0.31	0.20
$W_{\text{th}}$ (MJ)	7.14	2.02	0.93	2.90	0.82	2.75	4.24	1.59	3.12
$W_{\text{tot}}$ (MJ)	7.85	2.27	0.98	3.08	0.96	3.09	4.89	1.87	3.87
$t_{\text{saw}}$ (s)	55.3	52.9	63.0	54.5	62.0	55.3	57.8	57.2	56.4
Diagnostic time (s)	55.69	56.50	63.76	55.85	65.00	55.38	58.12	57.40	56.61

( $\nu_*$ ) scan, 5 discharges in which the isotope mass was varied, and a discharge referred to as an ‘‘identity shot.’’ Plasma parameters for these discharges are listed in Tables II and III. In the  $\rho_*$  scans,  $\rho_*$  was varied by a factor of 1.6 while all other dimensionless parameters (notably  $q$ , normalized collisionality  $\nu_*$ , and  $\beta$ ) were held nearly fixed<sup>15,16</sup> with only slight differences in these parameters within each scan. In addition, there were various amplitudes, frequencies, and types of ELMs at the edges of the plasmas in the discharges considered.

The first pair of discharges from the  $\rho_*$  scan, 33140 and 33131, have a heating power near the  $H$ -mode power threshold. The temperature and density profiles for these discharges are shown in Figs. 1 and 2. The global energy con-

finement scaling is observed to be Bohm-like in this scan.<sup>16</sup> The second pair, discharges 35171 and 35156, shown in Figs. 3 and 4, have heating power well above the  $H$ -mode threshold. These discharges are observed to follow a gyro-Bohm-like confinement scaling of  $B\tau_{\text{th}} \propto \rho_*^{-2.7}$  (where  $\tau_{\text{th}}$  is the global thermal energy confinement time), in agreement with ITER-93P scaling.<sup>17</sup> The ‘‘identity’’ discharge consid-

TABLE III. Major plasma parameters for the JET isotope scan discharges.

Tokamak discharge: Type	JET 42794 Tritium isotope	JET 42997 Tritium isotope	JET 43134 Deuterium isotope	JET 43443 Hydrogen isotope	JET 43452 Hydrogen isotope
$R$ (m)	2.95	2.95	2.95	2.95	2.95
$a$ (m)	0.80	0.80	0.80	0.80	0.80
$\kappa$	1.70	1.70	1.70	1.70	1.70
$\delta$	0.30	0.30	0.30	0.255	0.30
$B_T$ (T)	1.76	2.96	1.76	1.76	0.97
$I_p$ (MA)	1.78	1.78	1.78	1.77	0.97
$\bar{n}_e$ ( $10^{19} \text{ m}^{-3}$ )	5.39	4.84	4.36	2.56	2.57
$Z_{\text{eff}}$	3.36	3.17	2.53	1.46	2.09
$P_{\text{aux}}$ (MW)	6.74	10.4	7.40	7.40	7.40
$E_{\text{NBI}}$ (keV)	160.0	160.0	140.0	90.3	98.3
$\rho_*(0)$ ( $10^{-3} \text{ m}$ )	11.46	6.94	9.10	5.30	10.0
$\tau_{\text{th}}$ (s)	0.438	0.230	0.285	0.248	0.132
$W_{\text{th}}$ (MJ)	2.73	2.45	2.19	1.41	0.84
$W_{\text{tot}}$ (MJ)	3.19	3.12	2.75	1.81	1.00
$t_{\text{saw}}$ (s)	60.4	60.6	62.7	...	68.0
Diagnostic time (s)	60.6	60.84	62.9	62.1	69.6

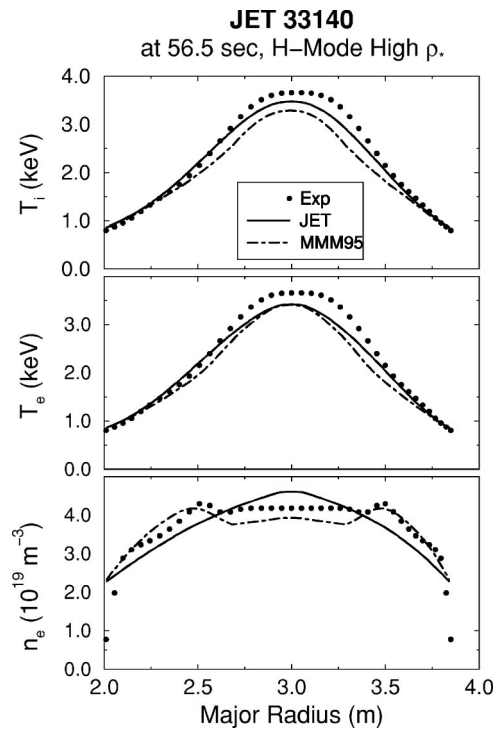


FIG. 1. Ion temperature, electron temperature, and electron density profiles as a function of major radius for simulations of the high  $\rho_*$  JET discharge 33140. In each panel, the closed circles represent experimental data, the solid curves are the results of simulations using the Mixed Bohm/gyro-Bohm model, and the dashed curves are simulations using the MMM95 model.

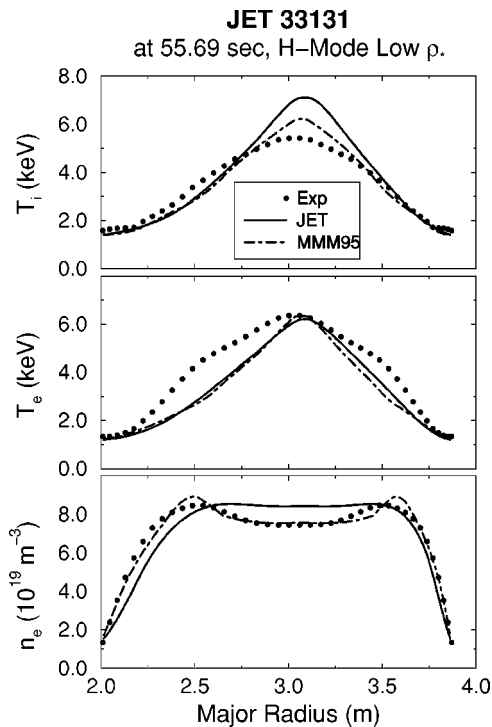


FIG. 2. Ion temperature, electron temperature, and electron density profiles as a function of major radius for simulations of the low  $\rho_*$  JET discharge 33131. In each panel, the closed circles represent experimental data, the solid curves are the results of simulations using the Mixed Bohm/gyro-Bohm model, and the dashed curves are simulations using the MMM95 model.

ered in this paper, JET 33465, is part of a series of experiments designed to test  $\rho_*$  scaling across various different tokamaks. All of these JET discharges were fueled with deuterium and heated by neutral beam injection. Discharge 33131, the low  $\rho_*$  experiment of the first pair, was additionally heated by 1.7 MW of absorbed ion cyclotron resonance heating, a relatively small component of the total heating of the plasma.

The next pair of JET discharges, 37718 and 37728, are taken from a scan in which the dimensionless collisionality (collision frequency divided by the bounce frequency) was varied by a factor of 2.6 while holding  $\rho_*$  and  $\beta$  fixed.<sup>4</sup> Discharge 37728 was heated with 1.1 MW of absorbed ion cyclotron resonance heating as well as 13.3 MW of neutral beam injected power. The final pair of JET discharges listed in Table II, 38407 and 38415, are taken from a scan in which the plasma beta was varied by a factor of 1.5 while holding  $\rho_*$  and the dimensionless collisionality fixed.<sup>4</sup> Finally, the 5 discharges listed in Table III are ELMy  $H$ -mode JET discharges in which different hydrogenic isotopes—hydrogen, deuterium, or tritium—were used for the plasma discharge and for the neutral beam injected gas.<sup>3</sup> The simulations for these discharges are compared with experimental data obtained directly from experimental measurements as described in Ref. 3.

Some of the discharges had irregularities complicating their study. For example, no information is available for the  $T_i$  profiles of JET discharges 33140, 33465, and 35171. The  $T_i$  profile data are set equal to  $T_e$  profile data for these dis-

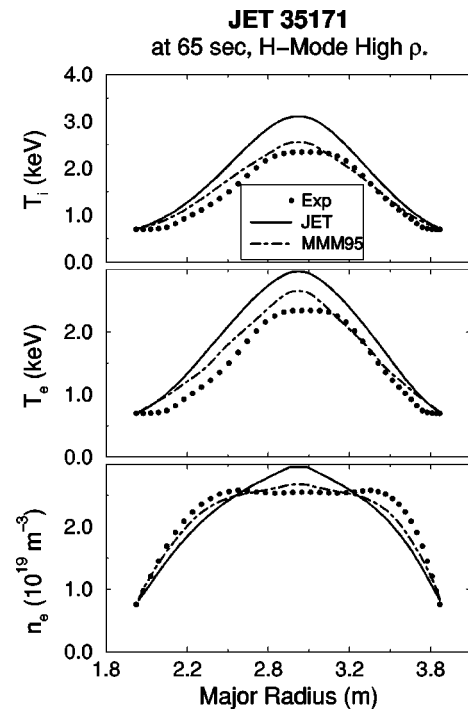


FIG. 3. Ion temperature, electron temperature, and electron density profiles as a function of major radius for simulations of the high  $\rho_*$  JET discharge 35171. In each panel, the closed circles represent experimental data, the solid curves are the results of simulations using the Mixed Bohm/gyro-Bohm model, and the dashed curves are simulations using the MMM95 model.

charges in the International Profile Database. The ion temperature profiles for these discharges are not used in the statistical analysis presented in Sec. IV A in the following. In addition, it was discovered that the diagnostic time of 65.87 s given in the International Profile Database for JET 35171 occurred after the beam heating power was turned off. To correct this, the diagnostic time was moved back to a relatively steady state period of the core discharge at 65.0 s, although the edges of the  $T_i$  and  $T_e$  profiles oscillate throughout the  $H$ -mode phase of the discharge. The diagnostic times for the other discharges are taken from the International Profile Database.

## B. DIII-D discharges

Four pairs of  $H$ -mode plasmas comprise the DIII-D discharges examined in this paper. Major plasma parameters for all 8 of the discharges taken from the International Profile Database are listed in Table IV. The discharges include scans for plasma power (77557 and 77559), density (81321 and 81329), elongation ( $\kappa$ ) (81499 and 81507), and  $\rho_*$  (82205 and 82788).

In the power scan experiment, the neutral beam injection power was varied while the average plasma density was kept constant. Power balance analysis shows that the thermal diffusivities increase with temperature, though the electron and ion diffusivities scale differently. At the half radius, electrons follow  $\chi_e \propto T_e^{3/2}$  and ions follow  $\chi_i \propto T_i$ .

In the density scan, the temperature was kept constant by increasing neutral beam injected power as the plasma density

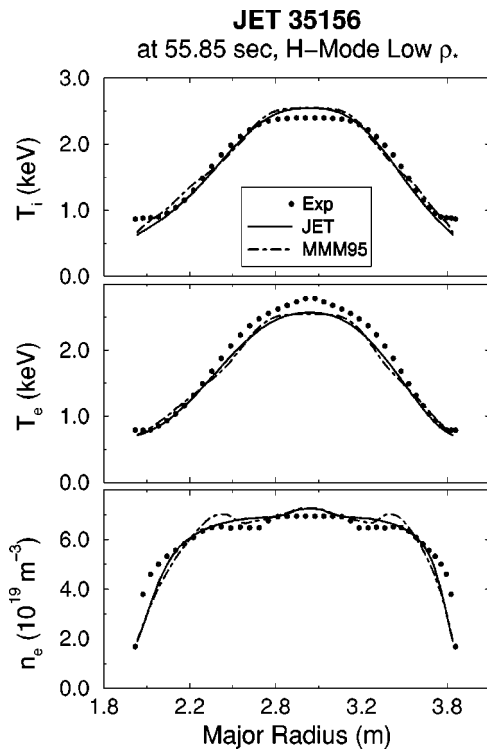


FIG. 4. Ion temperature, electron temperature, and electron density profiles as a function of major radius for simulations of the low  $\rho_*$  JET discharge 35156. In each panel, the closed circles represent experimental data, the solid curves are the results of simulations using the Mixed Bohm/gyro-Bohm model, and the dashed curves are simulations using the MMM95 model.

was increased. The diffusivities from power balance were found to be independent of the density of the plasmas in this scan.

The elongation scan tested a prediction<sup>18</sup> of better fusion performance in more elongated plasmas. If the plasma is stretched by lowering plasma width from the outside, while

the height, safety factor ( $q$ ), density, and heating power are kept fixed, the confinement of the plasma should not significantly change, according to global confinement scalings. Thus, an elongated plasma with smaller volume but the same density and stored energy (i.e., confinement  $\times$  power) will have higher temperatures than a less elongated plasma. As predicted, experimentalists observed higher temperatures in the more elongated plasma (discharge 81507). However, the degree of improved confinement exceeded the original prediction. The enhanced performance was attributed (at least in part) to an enhanced toroidal rotation gradient along the edge.

In the  $\rho_*$  scan, several dimensionless parameters such as elongation, plasma beta ( $\beta$ ), collisionality ( $\nu_*$ ), and  $q$ , were matched to the design specifications of ITER.<sup>19</sup> In both  $\rho_*$  discharges, the global thermal confinement time followed a gyro-Bohm scaling, as did the diffusivities from a power balance analysis. A confinement scaling with gyro-Bohm scaling yields a more optimistic confinement time and performance for ITER and similar fusion reactor designs than does a confinement scaling with Bohm scaling.

#### IV. SIMULATION RESULTS

Simulations are carried out using both the MMM95 and the JET model for each of the 22  $H$ -mode discharges and the resulting plasma profiles are compared with experimental data from the International Profile Database. Each pair of simulations is set up to be identical except for the choice of transport model. The time-dependent boundary conditions for these simulations (temperatures, densities, equilibrium boundary shape) as well as the time dependence of the average density and  $Z_{\text{eff}}$  are taken from the International Profile Database for these discharges.

A statistical analysis of the simulations compared with experimental data is described and applied in Sec. IV A to evaluate how well each of the two transport models match

TABLE IV. Major plasma parameters for the DIII-D discharges.

Tokamak discharge:	DIII-D 77557	DIII-D 77559	DIII-D 81321	DIII-D 81329	DIII-D 81499	DIII-D 81507	DIII-D 82205	DIII-D 82788
Type	Low power	High power	Low $n_e$	High $n_e$	Low $\kappa$	High $\kappa$	Low $\rho_*$	High $\rho_*$
$R$ (m)	1.68	1.69	1.69	1.70	1.69	1.61	1.69	1.68
$a$ (m)	0.62	0.62	0.60	0.59	0.63	0.54	0.63	0.62
$\kappa$	1.85	1.84	1.83	1.83	1.68	1.95	1.71	1.67
$\delta$	0.33	0.35	0.29	0.36	0.32	0.29	0.37	0.35
$B_T$ (T)	1.99	1.99	1.98	1.97	1.91	1.91	1.87	0.94
$I_p$ (MA)	1.00	1.00	1.00	1.00	1.35	1.34	1.34	0.66
$\bar{n}_e$ ( $10^{19} \text{ m}^{-3}$ )	4.88	5.02	2.94	5.35	4.81	4.90	5.34	2.86
$Z_{\text{eff}}$	1.68	2.21	2.42	1.65	2.33	1.93	2.13	1.94
$P_{\text{NB}}$ (MW)	4.73	13.23	3.49	8.34	5.74	5.71	5.86	3.25
$\rho_*(0)$ ( $10^{-3} \text{ m}$ )	11.02	14.30	12.38	12.09	12.01	16.43	13.04	19.36
$\tau_{\text{th}}$ (s)	0.11	0.06	0.12	0.08	0.12	0.11	0.14	0.06
$W_{\text{th}}$ (MJ)	0.58	0.88	0.41	0.69	0.72	0.66	0.84	0.20
$W_{\text{tot}}$ (MJ)	0.65	1.16	0.51	0.83	0.84	0.86	0.95	0.26
$t_{\text{saw}}$ (s)	2.63	2.66	3.87	1.50	3.81	2.45	0.36	2.06
Diagnostic time (s)	2.70	2.70	3.90	3.80	4.00	3.80	3.66	3.54

the data. The scaling and radial form of the diffusivities that result in the simulations using the JET transport model are considered in Sec. IV B, and it is shown that the Bohm component of the JET transport model dominates. Then, in Sec. IV C, a selection of JET  $\rho_*$  discharges is considered in detail in order to investigate the physical processes associated with the interplay between boundary conditions, sources and sinks, and transport in these simulations, with a particular emphasis on the gyroradius scaling of the transport models. Observations from the simulation of the scans carried out in the DIII-D tokamak are presented in Sec. IV D.

**A. Statistical analysis**

For each of the profiles (ion temperature, electron temperature, and electron density), we define the normalized deviation  $\epsilon_j$ , of the *j*th experimental data point  $X_j^{\text{expt}}$  and the simulation result  $X^{\text{sim}}(R_j)$  at the major radius  $R_j$  of the corresponding experimental data point as

$$\epsilon_j \equiv \frac{X^{\text{sim}}(R_j) - X_j^{\text{expt}}}{X_{\text{max}}^{\text{expt}}} \tag{7}$$

Note that each deviation is normalized by the maximum experimentally measured value for that given profile,  $X_{\text{max}}^{\text{expt}}$ , so that all the deviations have equal weight—rather than normalizing by the local experimental data point, which would over-weight the deviations near the edge of the plasma where the data points have small values.

For each profile at the diagnostic time for each discharge, we define the rms deviation  $\sigma$  and the offset *f* between the profile resulting from the simulation and the corresponding experimental data as

$$\sigma = \sqrt{\frac{1}{N} \sum_{j=1}^N \epsilon_j^2} \tag{8}$$

and

$$f = \frac{1}{N} \sum_{j=1}^N \epsilon_j \tag{9}$$

where *N* is the number of experimental data points in a profile. The rms deviation  $\sigma$  and the offset *f* are evaluated for each of the three profiles—ion temperature, electron temperature, and electron density—for the discharges considered. Note that the offset is positive if the simulated profile is systematically higher than the experimental profile and negative if the simulated profile is systematically lower than the experimental profile. If the offset is zero, then the rms deviation is a measure of how much the shapes of the profiles differ between simulation and experiment. The results of the statistical analyses are presented in Figs. 5–8 and in Table V.

The rms deviations and offsets for the ion temperature profiles for nineteen out of the 22 *H*-mode discharges that are simulated using the JET and the MMM95 models are shown in Figs. 5 and 6. 3 of the 22 *H*-mode discharges were excluded (JET discharges 33140, 33465, and 35171) because the ion temperatures in those 3 discharges were not measured (the ion temperatures were set equal to the electron temperatures in the International Profile Database). The rms devia-

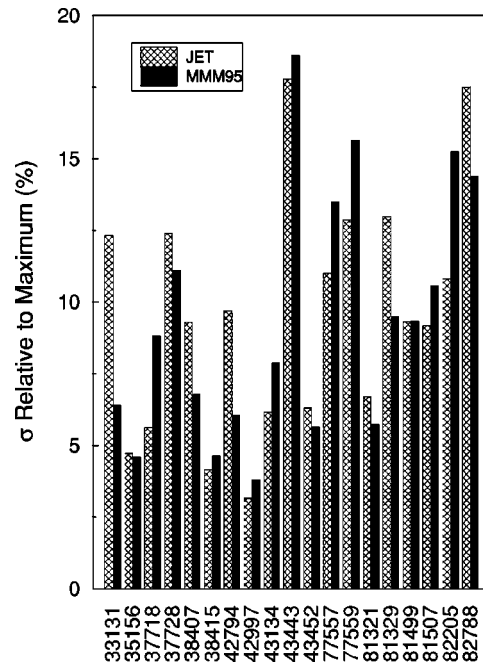


FIG. 5. Relative rms deviations (%) for the ion temperature profiles produced by simulations using the JET and MMM95 models compared with experimental data for 19 *H*-mode discharges listed by DIII-D and JET discharge number.

tions range from 4.6% to 17.8%, with no systematic trend that favors either model. The offsets are mostly negative, indicating that simulations underpredict the experimental data, but the negative values are 12% or less.

The average rms deviation  $\sigma_{\text{avg}}$  and average offset  $f_{\text{avg}}$ , averaged over 19 discharges for the ion temperature, and averaged over all 22 discharges for the electron temperature

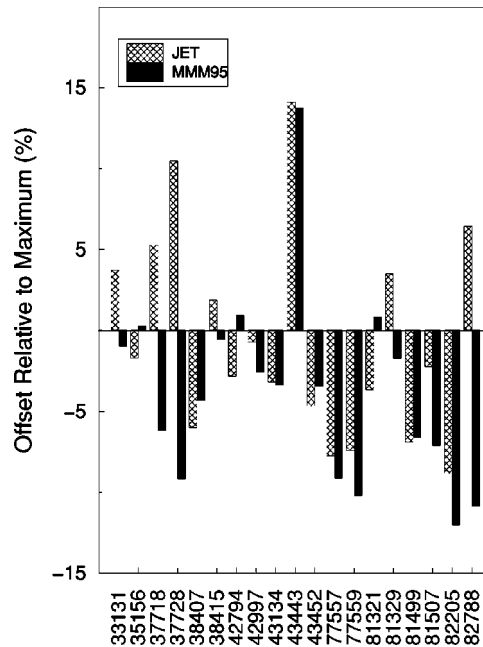


FIG. 6. Relative offset from for the ion temperature profiles produced by simulations using the JET and MMM95 models compared with experimental data for 19 *H*-mode discharges listed by DIII-D and JET discharge number.

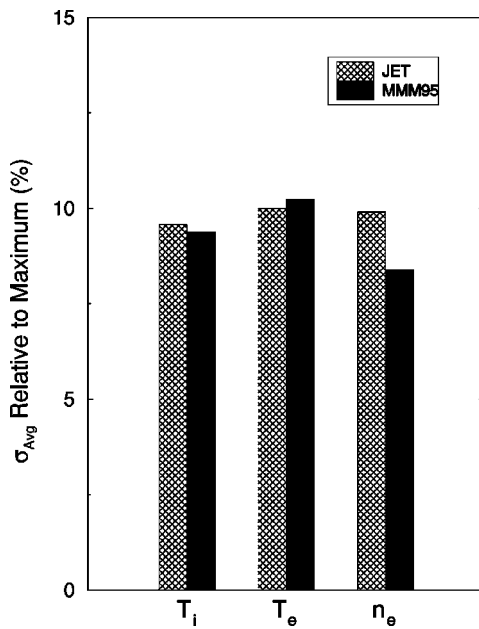


FIG. 7. Average rms deviation (%) for all three profiles produced by simulations using the JET and MMM95 models compared with experimental data for the 22  $H$ -mode discharges listed in Tables II and II.

and density profiles, are shown in Figs. 7 and 8 for the JET and the MMM95 transport model simulations. The average rms deviations differ by less than 1.6% between the two models for the three profiles, and the average offsets differ by less than 3.3%. The magnitudes of the average offsets for the JET transport model simulations are smaller than 2.5% for all three profiles while the magnitudes of the average offsets for the MMM95 model are less than 3.9% for all three profiles.

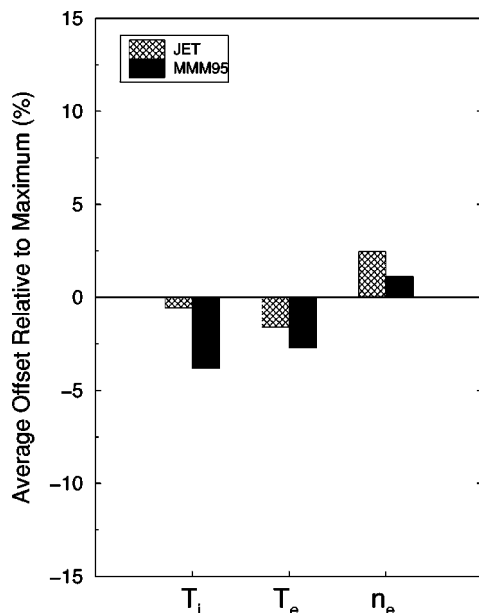


FIG. 8. Average offset from experiment (%) for all three profiles produced by simulations using the JET and MMM95 models compared with experimental data for the 22  $H$ -mode discharges listed in Tables II and II.

TABLE V. Average rms deviation and the scatter in rms deviations for the 22  $H$ -mode discharges (19 discharges for  $T_i$ ) simulated using the MMM95 and JET models.

Statistic	$T_i$	$T_e$	$n_e$
JET (%)			
$\sigma_{\text{avg}}$	9.58	9.99	9.90
$\sigma_{\sigma}$	4.17	5.50	3.04
MMM95 (%)			
$\sigma_{\text{avg}}$	9.38	10.24	8.39
$\sigma_{\sigma}$	4.34	5.94	3.48
$\Delta\sigma_{\text{avg}}$	0.20	-0.24	1.51

In order to determine whether or not these differences are statistically significant, it is useful to compute a measure of the scatter in the rms deviations from one discharge to the next. The rms deviation of the rms deviations for any given profile,  $\sigma_{\sigma}$ , is defined by

$$\sigma_{\sigma} = \frac{1}{J-1} \sum_{j=1}^J (\sigma_j - \sigma_{\text{avg}})^2, \quad (10)$$

where  $J$  is the number of discharges. The results for  $\sigma_{\text{avg}}$  and  $\sigma_{\sigma}$  are given in Table V. The difference between the average rms deviations for the JET and MMM95 models is significantly less than sum of the  $\sigma_{\sigma}$  values for all three profiles. Similar results are found for the offsets. Hence the difference between simulation results produced by the two models is not statistically significant. We conclude that the two models match  $H$ -mode experimental data from these 22 discharges equally well.

## B. Gyroradius scaling of the JET transport model

The effective diffusivities as a function of minor radius from a simulation using the JET transport model for the high  $\rho_*$  JET tokamak discharge 33140 are shown in Fig. 9. (Note that the “effective” thermal diffusivity, for example, is defined as the heat flux divided by the density times temperature gradient—with no separate contribution for convection.) This simulation of the JET discharge 33140 matched experimental data quite well, as can be seen in Fig. 1. The total thermal diffusivities shown in Fig. 9 are the sum total of contributions from the Bohm and gyro-Bohm terms in the JET model as well as neoclassical transport, which has gyro-Bohm scaling. It can be seen in Fig. 9 that the Bohm contribution to the JET transport model is the dominant contribution to the ion thermal diffusivity over most of the plasma, and the dominant contribution to the electron thermal diffusivity over the outer half of the plasma, in the case of this simulation.

The normalized minor radii where the transition occurs from gyro-Bohm dominance to Bohm dominance in the electron and ion thermal diffusivities for simulations using the JET model are listed in Table VI for the 22 discharges simulated. For the ion thermal diffusivity, it can be seen that the Bohm contribution is larger than the gyro-Bohm contribution over the outer two-thirds of the plasma in JET simulations of the JET tokamak discharges and over almost all of the

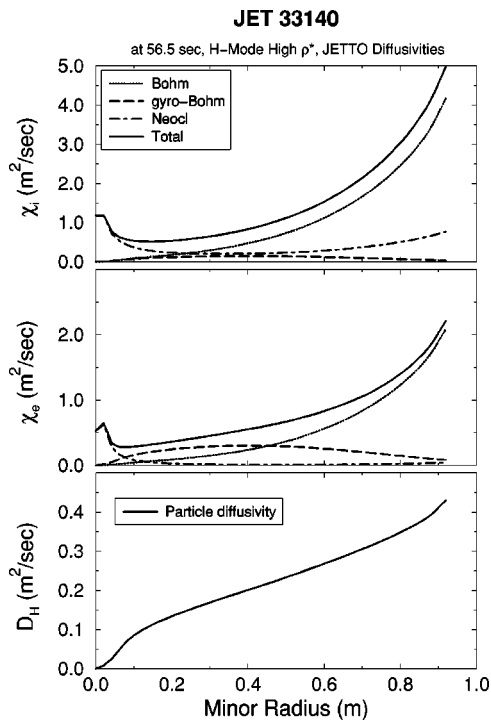


FIG. 9. Effective diffusivities as a function of minor radius from a simulation using the JET model for the high  $\rho_*$  JET discharge 33 140.

plasma in most of the DIII-D discharges. For the electron thermal diffusivity, the Bohm contribution is larger than the gyro-Bohm contribution over the outer half of the plasma in the simulations of JET discharges and the outer two-thirds of the plasma in most of the simulations of DIII-D discharges. The components of the thermal diffusivities shown in Fig. 9

TABLE VI. Normalized minor radius beyond which the Bohm component of the JET model is greater than the gyro-Bohm component in each simulation.

Tokamak	Discharge	$r/a$ for $\chi_e^{\text{Bohm}} > \chi_e^{\text{gyro-Bohm}}$	$r/a$ for $\chi_i^{\text{Bohm}} > \chi_i^{\text{gyro-Bohm}}$
JET	33131	0.48	0.40
JET	33140	0.46	0.10
JET	33465	0.48	0.20
JET	35156	0.41	0.30
JET	35171	0.47	0.23
JET	37718	0.57	0.00
JET	37728	0.64	0.25
JET	38407	0.45	0.05
JET	38415	0.43	0.05
JET	42794	0.71	0.07
JET	42997	0.65	0.00
JET	43134	0.66	0.07
JET	43443	0.25	0.00
JET	43452	0.57	0.05
DIII-D	77557	0.27	0.03
DIII-D	77559	0.27	0.05
DIII-D	81321	0.28	0.05
DIII-D	81329	0.28	0.05
DIII-D	81499	0.35	0.03
DIII-D	81507	0.33	0.03
DIII-D	82205	0.33	0.00
DIII-D	82788	0.41	0.27

are typical of the components of the JET transport model in all 22 discharges included in this study. The fact that the JET transport model has predominantly Bohm scaling while the multimode model has entirely gyro-Bohm scaling is a major fundamental difference between the models.

### C. Scaling of the $\rho_*$ scans in the JET tokamak

The JET and MMM95 model simulations of the 4 JET tokamak discharges, representing two gyroradius ( $\rho_*$ ) scans, are shown in Figs. 1–4. As noted in Sec. III A, the global energy confinement time is observed to have nearly Bohm scaling in discharges 33140 and 33131, while it has nearly gyro-Bohm scaling in discharges 35171 and 35156.<sup>4,16</sup> It is intriguing that simulations using transport models with such different gyroradius scaling (Bohm and gyro-Bohm) are able to match experimental data from two different  $H$ -mode  $\rho_*$  scans that have such different gyroradius scaling of global confinement.

The key to understanding how two transport models with different underlying scalings can both match two scans with different global confinement scalings is to examine the boundary conditions and the resulting shapes of the density and temperature profiles. Consider the pair of JET tokamak discharges 33140 and 33131 shown in Figs. 1 and 2, with plasma parameters given in Table II. The strength of the toroidal magnetic field was increased from 1.74 to 3.06 T as the scan progressed from discharge 33140 to 33131. In order to hold the average  $\beta$  and collisionality fixed in the discharges of this scan, the line averaged density was increased from 3.7 to  $7.1 \times 10^{19} \text{ m}^{-3}$  (proportional to  $B^{1.15}$ ) and additional heating was applied to increase the plasma thermal energy content from 2.0 to 7.3 MJ (proportional to  $B^{2.29}$ ).

However, the shapes of the electron density profiles near the edge of the plasma changes from relatively flat in the low field discharge 33140 to a relatively steeper gradient in the higher field discharge 33131, starting at the top of the  $H$ -mode pedestal in both cases. As a result, the pressure gradient near the edge of the plasma increases from the low field to the high field discharge. This has the effect of increasing the transport near the edge of the plasma in the high field case. This profile effect works against the gyroradius scaling, which would reduce the transport as the magnetic field is increased if the profile shapes were held fixed ( $\chi \propto B^{-1/3}$  for Bohm and  $\chi \propto B^{-1}$  for gyro-Bohm). The increase in thermal diffusivities near the edge of the plasma as the magnetic field is increased results in flatter temperature profiles near the edge of the plasma in the high field discharge 33131 (Fig. 2) relative to the low field discharge 33140 (Fig. 1). The variable  $\Delta T_e$  defined in Eq. (3), which serves as an estimate of the normalized temperature gradient, is reduced from 0.51 in the low field discharge 33140 to 0.38 in the high field discharge 33131.

The two transport models respond somewhat differently to the changes in the shapes of the profiles. The Bohm contribution to the thermal diffusivities of the JET transport model is proportional to the local electron pressure gradient multiplied by  $\Delta T_e$  from the edge of the plasma. As noted,  $\Delta T_e$  decreases with magnetic field while the dependence on

local electron pressure gradient gives the JET model some stiffness. Also, it can be seen from Table VI that the normalized radius at which the Bohm component becomes larger than the gyro-Bohm component of the ion thermal diffusivity moves from 0.1 in the low field discharge 33140 to 0.4 in the high field discharge 33131. These effects combine in the JET simulations to make the predicted energy confinement time nearly independent of magnetic field ( $\tau_E \propto B^{0.08}$ ).

The MMM95 transport model is somewhat stiffer than the JET transport model (the diffusivities increase more rapidly with increasing normalized temperature gradient in the plasma core). As a result, the flatter temperature gradient near the edge of the high field discharge 33131 has the effect of holding down all the rest of the temperature profile. This causes the predicted global energy confinement time to be nearly independent of magnetic field, ( $\tau_E \propto B^{0.11}$ ) even though the underlying gyro-Bohm scaling of MMM95 would predict confinement proportional to magnetic field if the profiles were actually held fixed.

The change in the normalized edge density gradient is less pronounced in the other JET  $\rho_*$  scan, 35171 (Fig. 3) and 35156 (Fig. 4). In that scan, the edge densities increase with magnetic field ( $n_{\text{edge}} \propto B^{1.05}$ ) in a way that is more consistent with the increase of the line averaged density ( $\bar{n}_e \propto B^{1.52}$ ). As a result, the normalized edge electron pressure gradient increases by a factor of 2.0 from the low field discharge 35171 to the high field discharge 35156, compared with the much larger increase by a factor of 6.9 in the other  $\rho_*$  scan described previously. Throughout the core of the plasma, the normalized shapes of the density and temperature profiles are more peaked in the low field discharge 35171 than they are in the high field discharge 35156. These changes in the shapes of the profiles together with the underlying scaling of the transport models causes the predicted global thermal energy confinement time,  $\tau_{\text{th}}$ , to increase significantly with magnetic field strength ( $\tau_{\text{th}} \propto B^{0.54}$  for the JET transport model and  $\tau_{\text{th}} \propto B^{0.81}$  for the MMM95 transport model) in this JET tokamak  $\rho_*$  scan.

#### D. DIII-D scans

Simulations were carried out using the JET and MMM95 transport models for the 8 DIII-D discharges listed in Table IV. These discharges represent scans in heating power (77557 and 77559), density (81321 and 81329), elongation (81499 and 81507), and normalized gyroradius,  $\rho_*$  (82788 and 82205). The rms deviations and relative offsets are shown for the 8 discharges on the right hand side of Figs. 5 and 6.

First, consider the DIII-D  $\rho_*$  scan represented by discharges 82788 and 82205. The energy confinement time ( $\tau_E \equiv W_{\text{tot}}/P_{\text{NB}}$ ) computed from the experimental data has gyro-Bohm scaling  $\tau_E \propto B^{1.03}$  for this set of discharges. The energy confinement time from the simulations using the MMM95 transport model is found to be close to gyro-Bohm scaling ( $\tau_E \propto B^{0.90}$ ), while the energy confinement time from the simulations using the JET transport model is found to have a scaling between gyro-Bohm and Bohm ( $\tau_E \propto B^{0.67}$ ). In particular, the MMM95 model underpredicted both tem-

perature profiles in both discharges while the JET model overpredicted both temperature profiles in the high  $\rho_*$  discharge 82788 and underpredicted both temperature profiles in the low  $\rho_*$  discharge 82205, although this difference is still not statistically significant.

It is found that there is no systematic trend in the power scan (discharges 77557 and 77559). Both models underpredicted the ion temperature profiles by about the same amount and both models predicted the electron temperature profiles more accurately. The MMM95 thermal diffusivities increase with electron temperature ( $\chi \propto T_e^{3/2}$ ) and also the contributions to the thermal diffusivity from different parts of the MMM95 model increase with normalized ion temperature gradient (for the drift modes) or with normalized pressure gradient (for the ballooning modes). The thermal diffusivities, which result when the JET transport model is used, also increase with electron temperature ( $\chi \propto T_e$  for the Bohm contribution) and with the normalized electron pressure gradient. All of these dependencies contribute to the observed scaling of confinement with respect to heating power.

In the density scan (discharges 81321 and 81329), the heating power was adjusted to hold the temperatures fixed as the plasma density was increased. The simulations using both models matched the experimental data quite well for both discharges in this scan, as shown in Figs. 10 and 11. The shapes of all the profiles remained nearly the same in the two discharges of this scan, in both the experimental data and in the simulations (except for some structure in the density profile). If the magnitudes and normalized shapes of the profiles are fixed from one discharge to another, then the diffusivities predicted by both the JET and MMM95 models remain nearly fixed.

In the DIII-D elongation scan (discharges 81499 and 81507), the plasma elongation (at the 95% flux surface) is increased from 1.68 to 1.95 while the width of the plasma is decreased from 0.63 to 0.54 m. It can be seen from the data in Table IV that the energy confinement time  $\tau_E \equiv W_{\text{tot}}/P_{\text{NB}}$  changed by only 3% (0.146 to 0.151 s). Similar results are found in the simulations: The energy confinement time decreased by only 1.3% (from 0.161 to 0.159) in the simulation using the JET transport model, and it increased by only 5.5% (from 0.145 to 0.153) in the simulation using the MMM95 transport model. Any effect that elongation has on the transport model is offset by the reduction of the width of the plasma which increases the temperature and density gradients across the width of the plasma.

In many of the simulations of the DIII-D discharges using the JET model, especially in those with higher neutral beam heating power and, consequently, higher neutral beam fueling, there is a central peak in the electron density profiles that is not present in the experimental data. This observation suggests that the JET transport model is predicting too little charged particle transport near the magnetic axis.

#### V. ITER SIMULATIONS

It has been demonstrated in this paper that BALDUR simulations using the JET and MMM95 transport models match *H*-mode experimental data equally well on average for

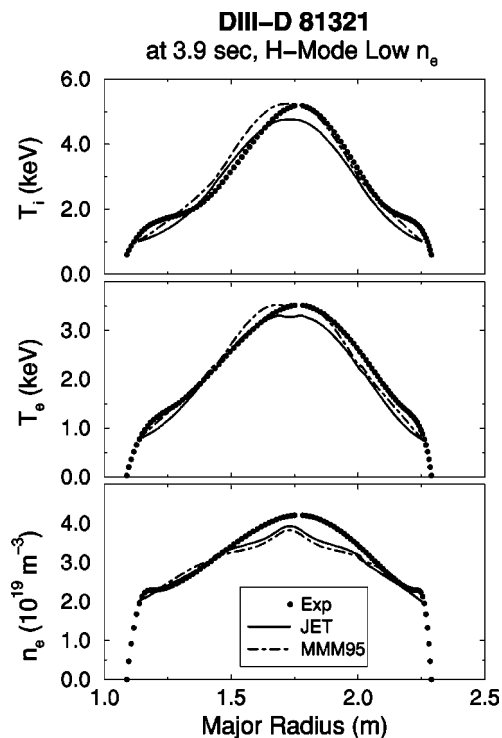


FIG. 10. Ion temperature, electron temperature, and electron density profiles as a function of major radius for simulations of the low density DIII-D discharge 81321. In each panel, the closed circles represent experimental data, the solid curves are the results of simulations using the Mixed Bohm/gyro-Bohm model, and the dashed curves are simulations using the MMM95 model.

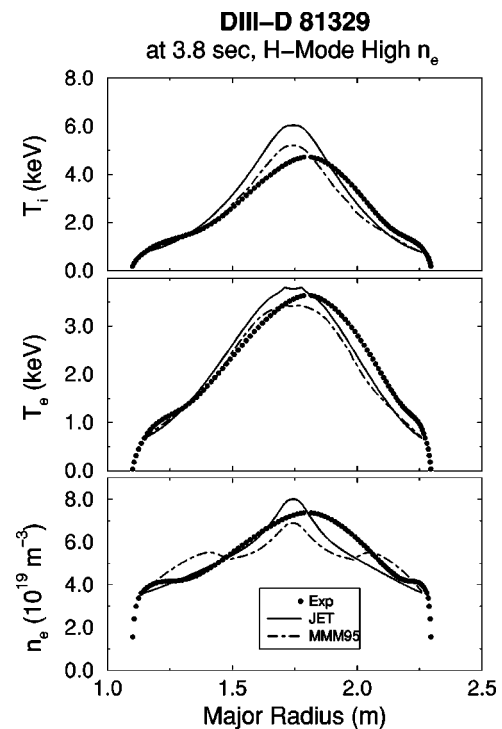


FIG. 11. Ion temperature, electron temperature, and electron density profiles as a function of major radius for simulations of the high density DIII-D discharge 81329. In each panel, the closed circles represent experimental data, the solid curves are the results of simulations using the Mixed Bohm/gyro-Bohm model, and the dashed curves are simulations using the MMM95 model.

all the discharges considered, including the  $\rho_*$  scans. Now it would be useful to compare simulations of a fusion reactor design using these two models. Systematic scans of simulations using the MMM95 model have been published for the original design of the International Thermonuclear Experimental Reactor (ITER).<sup>20,19</sup> That version of the ITER design had the following engineering parameters: major radius  $R = 8.14$  m, minor radius  $a = 2.80$  m, elongation  $\kappa = 1.60$ , triangularity  $\delta = 0.24$ , toroidal magnetic field  $B_t = 5.68$  T, plasma current  $I_p = 21.0$  MA, and the volume-averaged effective ion charge  $\langle Z_{\text{eff}} \rangle = 1.5$ .

Figure 12 shows the alpha heating power as a function of time for a selection of edge temperatures from simulations using the JET transport model with volume averaged electron densities rising to  $1.1 \times 10^{20}$  (top panel) and  $0.9 \times 10^{20} \text{ m}^{-3}$  (bottom panel). In these time-dependent simulations, 100 MW of neutral beam injection with 1 MeV deuterium atoms is applied from 90 to 150 s. The alpha heating power remains high after the auxiliary heating is turned off at 150 s (indicating ignition) in those simulations with edge temperatures that are 3 keV or higher, while the alpha heating power decays rapidly (not igniting) when the edge temperature is 2.5 keV or less. The pulses of alpha power are associated with sawtooth oscillations in these simulations.

Simulations of ITER, using the JET transport model, show that ITER would ignite when the edge temperature is about 3 keV or higher and the volume averaged density is  $0.9 \times 10^{20} \text{ m}^{-3}$  or higher, with  $Z_{\text{eff}} = 1.5$  from carbon and ac-

cumulated helium (see Fig. 12). Simulations set up in the same way using the MMM95 model rather than the JET transport model (i.e., with the same boundary conditions, auxiliary heating, and density ramp) ignited with edge temperatures as low as 0.25 keV or with volume average density as low as  $0.775 \times 10^{20} \text{ m}^{-3}$ .<sup>20</sup> The only dimensionless parameters that are different between ITER and present day tokamaks such as JET or DIII-D are the normalized gyroradius  $\rho_*$  and the atomic physics scale lengths, such as the normalized penetration length for edge neutrals. The gyroradius scaling of the JET model is dominated by Bohm scaling, which is more pessimistic than the gyro-Bohm scaling of the MMM95 model, when extrapolated from present-day experiments to fusion reactors. That is, Bohm scaling of confinement increases more slowly with size and magnetic field than does gyro-Bohm scaling.

## VI. CONCLUSION

Predictive transport simulations of 22  $H$ -mode discharges in JET and DIII-D have been carried out with the JET and with the MMM95 transport models. A statistical analysis indicates that the temperature and density profiles from simulations using both models match experimental data equally well. On average, the MMM95 model underpredicted the temperature profiles by 3% or 4% more than the JET transport model, but that difference is not statistically significant. The average rms deviations are about 9% or 10% for both models.

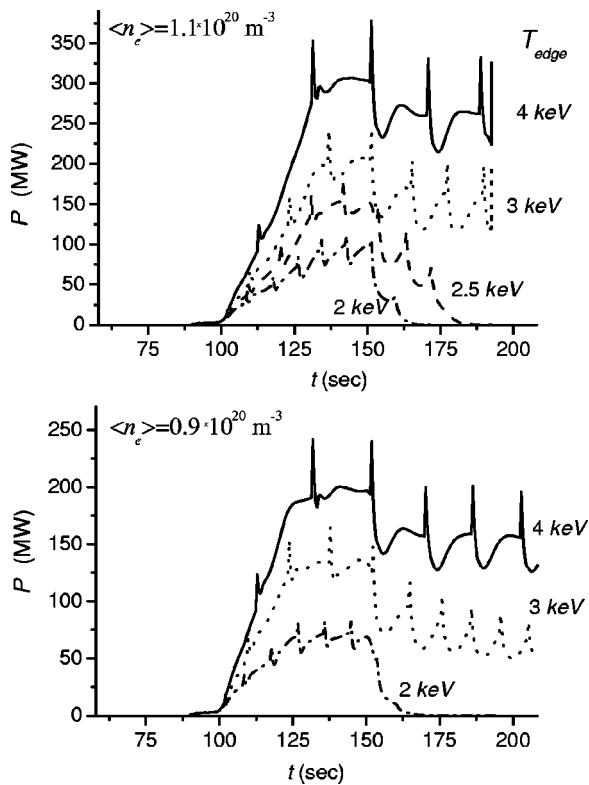


FIG. 12. Alpha heating power from simulations of ITER using the JET transport model for  $\langle n_{e20} \rangle = 1.1$  (top panel) and  $\langle n_{e20} \rangle = 0.9$  (bottom panel). In each panel, the curves show results from simulations using an edge temperature of 4.0 keV (top curve), 3.0 keV (second curve), 2.5 keV (third curve in the left panel only), and 2.0 keV (bottom curve).

The two transport models have different gyroradius scaling—the JET model has predominantly Bohm scaling over most of the outer regions of the plasma in these simulations, while the MMM95 model has purely gyro-Bohm scaling. There are also significant differences between the internal structures of the models. The Bohm contribution to the JET transport model, for example, has a nonlocal factor that causes the transport throughout the plasma to depend on the normalized electron temperature gradient at the edge of the plasma. The MMM95 transport model depends entirely on local plasma parameters, with a rather stiff dependence on the normalized ion temperature gradient. In spite of these differences, simulations using both models matched the trends observed in the experimental data in systematic scans over gyroradius, plasma power, density, and elongation. However, simulations of the ITER fusion reactor design using the JET transport model required higher edge temperature (about 3 keV) to ignite than corresponding simulations using the MMM95 model, which would ignite with only a 0.25 keV edge temperature.

The simulations presented in this paper illustrate the following basic principle: Global confinement scalings are determined by the shapes of the plasma profiles in addition to the underlying scaling of the transport model. The shapes of the plasma profiles (including densities, temperatures, current, and flow) are determined by the effects of boundary conditions, profiles of sources and sinks, large scale instabilities, as well as transport. Boundary conditions, for example, were shown to have a significant effect on the shapes of the density and temperature profiles and, consequently, a significant effect on the scaling of confinement in the systematic scans presented in this paper.

## ACKNOWLEDGMENTS

This work was funded by National Science Foundation Grant No. PHY 9820301 and Department of Energy Grant No. DE-FG02-92-ER-54141.

- <sup>1</sup>G. Bateman, A. H. Kritz, J. E. Kinsey, A. J. Redd, and J. Weiland, *Phys. Plasmas* **5**, 1793 (1998).
- <sup>2</sup>P. H. Rebut *et al.*, *Nucl. Fusion* **25**, 1011 (1985).
- <sup>3</sup>G. Bateman, A. H. Kritz, V. V. Parail *et al.*, *Phys. Plasmas* **6**, 4607 (1999).
- <sup>4</sup>J. E. Kinsey, *Nucl. Fusion* **39**, 539 (1999).
- <sup>5</sup>G. Bateman *et al.*, in *Proceedings of the Sixteenth IAEA Fusion Energy Conference, Montréal, Canada, 7–11 October 1996* (IAEA, Vienna, 1996), Vol. II, pp. 559–565.
- <sup>6</sup>J. E. Kinsey and G. Bateman, *Phys. Plasmas* **3**, 3344 (1996).
- <sup>7</sup>M. Erba, T. Aniel, V. Basiuk, E. Becoulet, and X. Litaudon, *Nucl. Fusion* **38**, 1013 (1998).
- <sup>8</sup>D. Boucher *et al.*, *Nucl. Fusion* **40**, 1955 (2000).
- <sup>9</sup>C. E. Singer, D. E. Post, D. R. Mikkelsen *et al.*, *Comput. Phys. Commun.* **49**, 275 (1988).
- <sup>10</sup>J. L. Luxon and L. G. Davis, *Fusion Technol.* **8**, 441 (1985).
- <sup>11</sup>A. H. Kritz *et al.*, in *European Physical Society Meeting, Kiev, Ukraine, 13 June 1996* (European Physical Society, Petit-Lancy, 1996).
- <sup>12</sup>J. E. Kinsey, R. E. Waltz, and D. P. Schissel, in *European Physical Society Meeting, Berchtesgaten, Germany, June 1997* (European Physical Society, Petit-Lancy, Switzerland, 1998).
- <sup>13</sup>J. E. Kinsey, G. Bateman, A. H. Kritz, and A. Redd, *Phys. Plasmas* **3**, 561 (1996).
- <sup>14</sup>R. J. Hawryluk *et al.*, *Fusion Technol.* **30**, 648 (1996).
- <sup>15</sup>B. Balet *et al.*, *Proceedings of the 22nd European Conference Bournemouth, 1995* (European Physical Society, Geneva, 1995), Vol. 19C, p. 935, Part I.
- <sup>16</sup>J. G. Cordey *et al.*, *Plasma Phys. Controlled Fusion* **38**, A67 (1996).
- <sup>17</sup>ITER Confinement Database and Modeling Group (presented by S. M. Kaye), in *Proceedings of the 15th International Conference Seville, 1994* (IAEA, Vienna, 1995), Vol. 2, p. 525.
- <sup>18</sup>C. M. Greenfield, J. C. DeBoo, T. H. Osborne, F. W. Perkins, M. N. Rosenbluth, and D. Boucher, *Nucl. Fusion* **37**, 1215 (1997).
- <sup>19</sup>ITER Physics Basis Editors *et al.*, *Nucl. Fusion* **39**, 2175 (1999).
- <sup>20</sup>G. Bateman, A. H. Kritz, J. E. Kinsey, and A. J. Redd, *Phys. Plasmas* **5**, 2355 (1998).